Electronic Supporting Information

From one to two: In-site constructing C_3N_5-Poly (triazine imide) heterojunction for enhanced O_2 activation

Shiling Xu,[a] Ziheng Yang,[a] Laiqing Zhang,[a] Xiaorui Zhang,[a] Zikang Zeng,[a] Wenxuan Wang,[a] Yujun Liang,[a] Lan Yuan*[b] and Chuang Han*[a]*

[a]Faculty of Materials Science and Chemistry, China University of Geosciences, Wuhan 430074, China

[b]School of Chemistry and Chemical Engineering, Wuhan University of Science and Technology, Wuhan 430081, China

*Corresponding author, E-mail: yujunliang@sohu.com (Yujun Liang); yuanlan@wust.edu.cn (Lan Yuan) hanc@cug.edu.cn (Chuang Han)

Contents list:

Experimental Section
Fig. S1 The SEM image of (a) C_3N_5. (b) PTI
Fig. S2 TEM images of (a) C_3N_5-PTI and (b) C_3N_5. (c) HR-TEM images of C_3N_5-PTI.
Fig. S3 N_2 adsorption-desorption isotherms.
Fig. S4 (a) X-ray photoelectron spectra (XPS) of C_3N_5, PTI and C_3N_5-PTI. (b) FT-IR spectra of C_3N_5, C_3N_5-PTI and PTI.
Fig. S5 Kubelka-Munk plots of (a) C_3N_5 and (b) PTI. Mott-Schottky curves of (c) C_3N_5 and (d) PTI.
Fig. S6 Band structure alignment of C_3N_5 and PTI.
Fig. S7 (a) ESR spectra of C_3N_5-PTI, PTI and C_3N_5 obtained in the presence of DMPO as an electron-trapping agent. (b) Photoluminescence (PL) spectra of as-samples in the presence of terephthalic acid (excitation wavelength: 320 nm). (c) The degradation of DPBF in C_3N_5, PTI and C_3N_5-PTI systems.
Fig. S8 (a) The UPS spectra of C_3N_5 and PTI, (b) Schematic illustration of the band positions for C_3N_5 and PTI.
Fig. S9 K_f, K_d fitting curve of (a) C_3N_5-PTI, (b) PTI and (c) C_3N_5, (d) H_2O_2 decomposition rate of the prepared samples. ($y=[H_2O_2]$, $a=K_f/K_d$, $b=K_d$)
Fig. S10 (a) The linear relationship of concentration of H_2O_2 vs. UV-vis absorbance and (b) Standard curves for different concentration of H_2O_2
Equation S1-2.
Table S1. Surface area and pore information of the prepared samples.
Table S2. Comparison of photocatalytic H_2O_2 yields over different semiconductor catalysts.
References

Experimental Section:

Materials. 3-amino-1,2,4-triazole (3-AT, 99%, Energy Chemical), Potassium chloride (KCl, AR, Sinopharm), Lithium chloride (LiCl, 99%, Meryer), Potassium iodide (KI, AR, Sinopharm), Ammonium molybdate hydrate ($H_{32}Mo_7N_6O_{28}$, 99%, Energy Chemical), Ethanol (C_2H_5OH, AR, Sinopharm), Hydrogen peroxide (30% H_2O_2, AR, Sinopharm), Silver nitrate ($AgNO_3$, AR, Sinopharm), P-benzoquinone (p-BQ, AR, Sinopharm), 1,3-Diphenylisobenzofuran (DPBF, 96%, Bide), Terephthalic acid (TPA, 99%, Energy Chemical)

Preparation.

(I) Preparation of C_3N_5-PTI heterojunction nanomaterials

The C_3N_5-PTI heterojunction was synthesized by two-step thermal polycondensation of 3-amino-1,2,4-triazole (3-AT) with KCl and LiCl. 3-AT (2 g) was heated to 520 °C for 3 h at a rate of 3 °C/min in a muffle furnace. Then, 0.6 g sample was ground entirely with 6 g eutectic salt mixture of 2.7 g LiCl and 3.3 g KCl for 20 min. Next, the mixture was calcined to 500 °C for 3 h at a rate of 3 °C /min in a crucible under air. Following that, the collected samples were ground fully and followed by washing twice alternately with hot deionized water and ethanol to ensure the removal of remaining salts. Subsequently, the sample was dried at 60 °C overnight.

(II) Preparation of C_3N_5

C_3N_5 was synthesized by thermal polymerization of 3-AT. A porcelain crucible was loaded with 3-AT(2 g) and calcined at 520 °C for 3 h in air at a heating rate of 10 °C/min.

(III) Preparation of poly triazine imide (PTI)

Poly triazine imide (PTI) photocatalyst was synthesized via molten salt methods. 2 g of 3-AT was ground completely with 5 g eutectic salt mixture of 2.26 g LiCl and 2.74 g KCl for 20 min. Then, the mixture was calcined to 600 °C for 3 h at a rate of 10 °C /min in a crucible under air. The subsequent procedure was similar to C_3N_5-PTI.

Characterization.

The phase and crystal structure of as-samples were observed by X-ray diffraction (XRD, AXS D8-Focus, Bruker, Germany) with the 2θ range from 5° to 60°. The morphology and microstructure of the samples were observed by transmission electron microscopy (TEM, Talos F200x, Thermo Fisher Scientific) and field emission scanning electron microscope (FE-SEM, SU8010, Hitachi, Japan). Elemental maps and energy dispersive (EDS) spectra of the catalysts were obtained by scanning electron microscopy. The X-ray photoelectron spectroscopy (XPS, K-alpha, Thermo Scientific, America) spectra were applied to analyze the element compositions and chemical states. The pore size, pore volume, and surface area of samples were obtained by the Brunauer-Emmett-Teller (BET, V-sorb 2800P, China) instrument. The light absorption characteristics of the prepared samples were analyzed by UV-Vis diffuse reflectance spectroscopy (DRS, UV-2550 PC). The photoluminescence (PL) spectra of the prepared samples were measured by a fluorescence spectrometer (Fluoromax- 4 P, Horiba Jobin Yvon), using an emission wavelength of 365 nm. The free radicals of $\bullet O_2^-$ were recorded on electron spin resonance (ESR, Bruker EMXplus-6/1) using DMPO as the spin-trapper agent. The electrochemical properties of samples were tested by an electrochemical workstation (CHI-760E,

Shanghai). The work function of samples was characterized by Ultraviolet photoelectron spectroscopy (UPS, PHI5000 VersaProbe III).

H_2O_2 detection

The photocatalytic hydrogen peroxide production reactions were performed under the 5W white LED lamp irradiation. In a typical operation, 5 mg of the photocatalysts were ultrasonically dissolved in 33 mL of aqueous solution containing 10 vol% ethanol by ultrasound. The obtained solution was stirred and air bubbled to obtain an oxygen environment. During the reaction, 2 mL of the suspension was collected every 15 min and the photocatalyst material was removed using a 0.22 μL nylon needle filter. H_2O_2 concentration was determined by the iodometric method. 1 mL of suspension was taken out and mixed with 2 mL of 0.1M KI and 0.05 mL of 0.01M $H_{32}Mo_7N_6O_{28}$ solution. The absorbance was detected by UV-vis diffuse reflectance spectra. The concentration of H_2O_2 was calculated by the equation given in **Fig. S10**.

H_2O_2 decomposition detection methods

The reaction conditions for the H_2O_2 decomposition experiments were referred to previous works with minor revisions.[1-3] Specifically, experiments were carried out by adding 5 mg of the photocatalyst samples to 1 mL 8 mM H_2O_2 solution without air bubbles. After 90 min of light exposure, 2 mL of the suspension was collected, and the photocatalytic material was removed using a 0.22 μL nylon needle filter. The H_2O_2 concentration was determined by the iodometric method and was used to assess the decomposition of H_2O_2 by UV-Vis reflectance spectra.

Electrochemical measurements

Electrochemical tests were performed on an electrochemical workstation (CHI-760E, Shanghai). The 10 mg catalyst was dispersed into 250 μL ethanol, followed by 20 μL Nafion solution (5 wt%), and then the mixture was ultrasonic for 20 min to achieve a homogeneous catalyst. Finally, the obtained catalyst was uniformly dripped onto the FTO conductive glass and dried to form a working electrode. Generally, the Ag/AgCl electrode is used as the reference electrode and the Pt wire as the counter electrode. 0.1 M Na_2SO_4 solution was used as the electrolyte and a 300 W xenon lamp was used as the light source. In addition, the impedance test was measured using 0.5 M KCl solution and 5mM $K_3[Fe(CN)_6]/K_4[Fe(CN)_6]$ as the electrolyte solution.

The position of the guide tape is calculated by the following formula:

$E_{CB}=E_{fb}-0.1$

$E_{NHE}=E_{(Ag/AgCl)}+0.197$

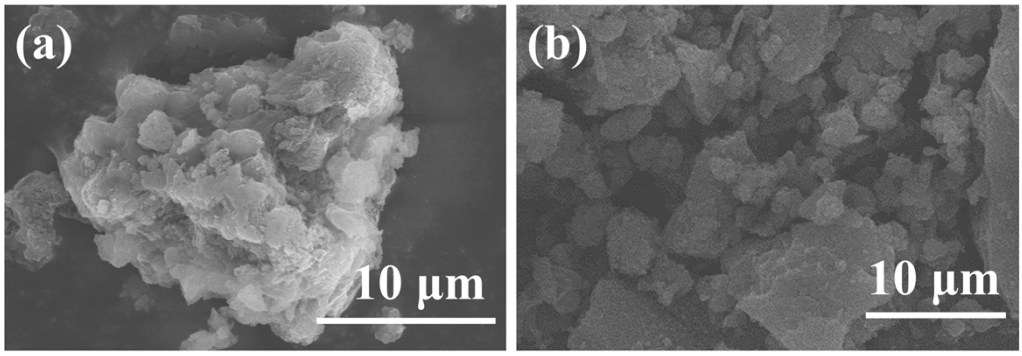

Fig. S1 The SEM image of (a) C_3N_5. (b) PTI

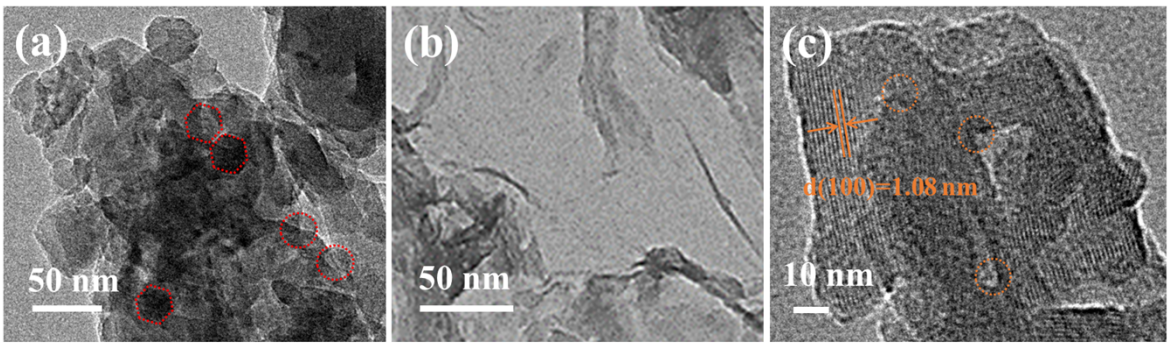

Fig. S2 TEM images of (a) C_3N_5-PTI and (b) C_3N_5. (c) HR-TEM images of C_3N_5-PTI.

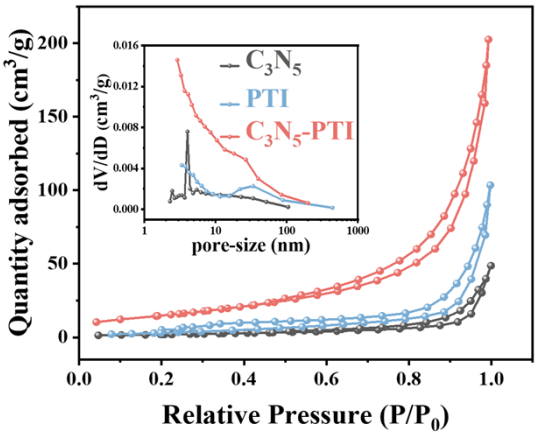

Fig. S3 N_2 adsorption-desorption isotherms.

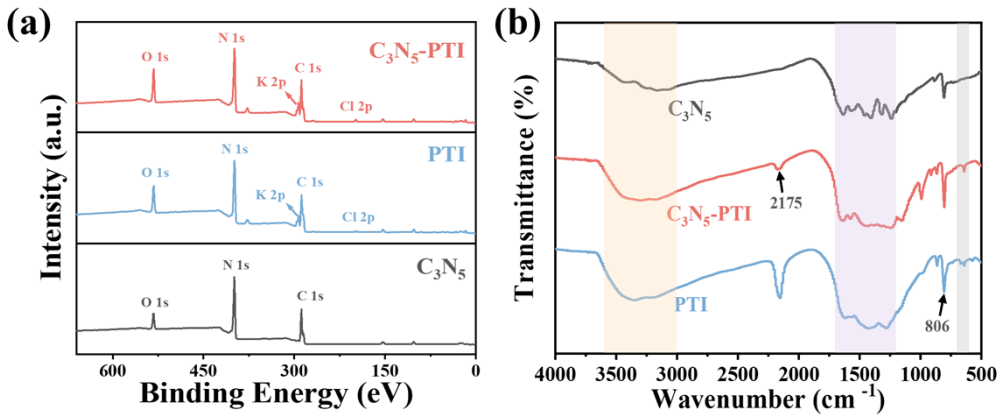

Fig. S4 (a) X-ray photoelectron spectra (XPS) of C_3N_5, PTI and C_3N_5-PTI. (b) FT-IR spectra of C_3N_5, C_3N_5-PTI and PTI.

Notes: As shown in Fig. S4b, the distinctive stretching vibrations at band locations of 600-700 cm^{-1} (shaded by grey) indicate the unique structure of the PTI.[4] The obvious adsorption peak at 806 cm^{-1} corresponded to the out-of-plane bending vibration of the heptazine units,[5] while the broad peaks in the range of 3000-3600 cm^{-1} (shaded by orange) were assignable to the absorbed H_2O molecules and terminal amino groups.[6] Furthermore, the stretching vibration modes of C-N heterocycles were the source of the strongest absorption bands in the 1200-1700 cm^{-1} area.[7] Notably, the spectra of the C_3N_5-PTI and PTI showed a clear peak at 2175 cm^{-1}, which was attributed to the terminal cyano groups (-C≡N) produced by the 3-AT following ammonia loss during calcination in the alkali metal chloride molten solution.[8]

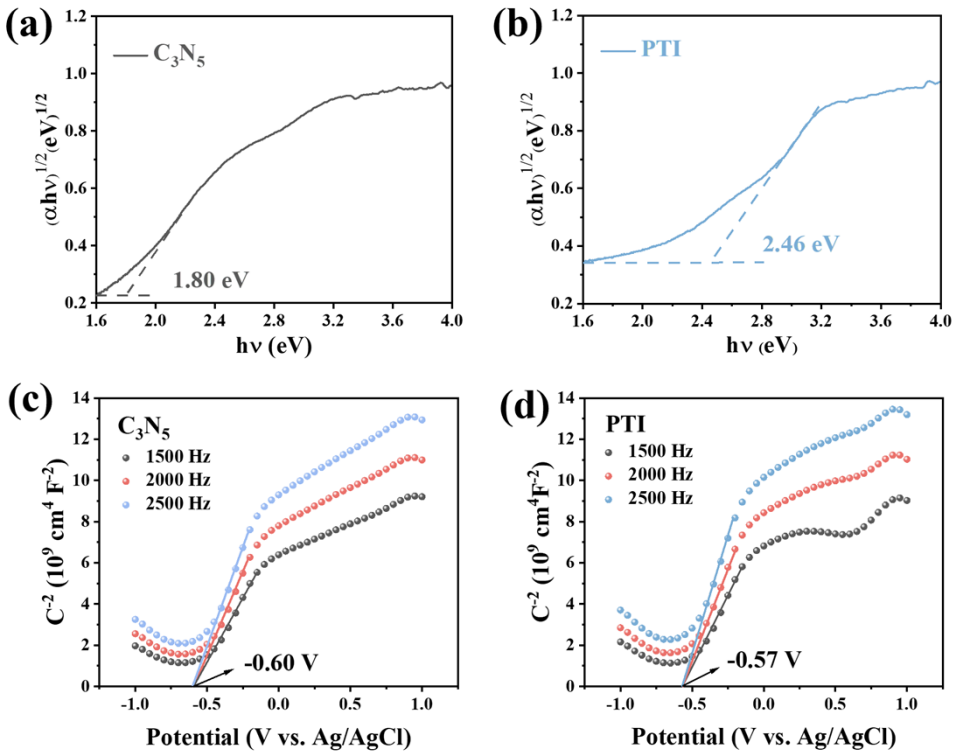

Fig. S5 Kubelka-Munk plots of (a) C_3N_5 and (b) PTI. Mott-Schottky curves of (c) C_3N_5 and (d) PTI.

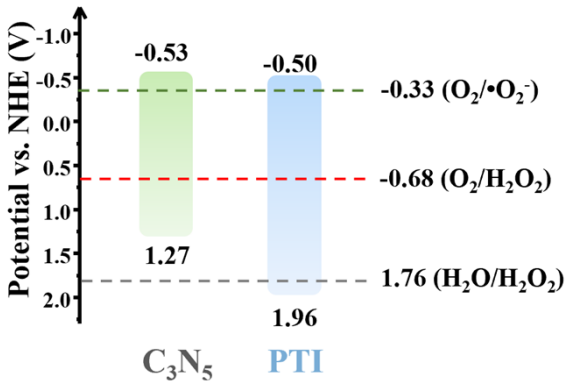

Fig. S6 Band structure alignment of C_3N_5 and PTI.

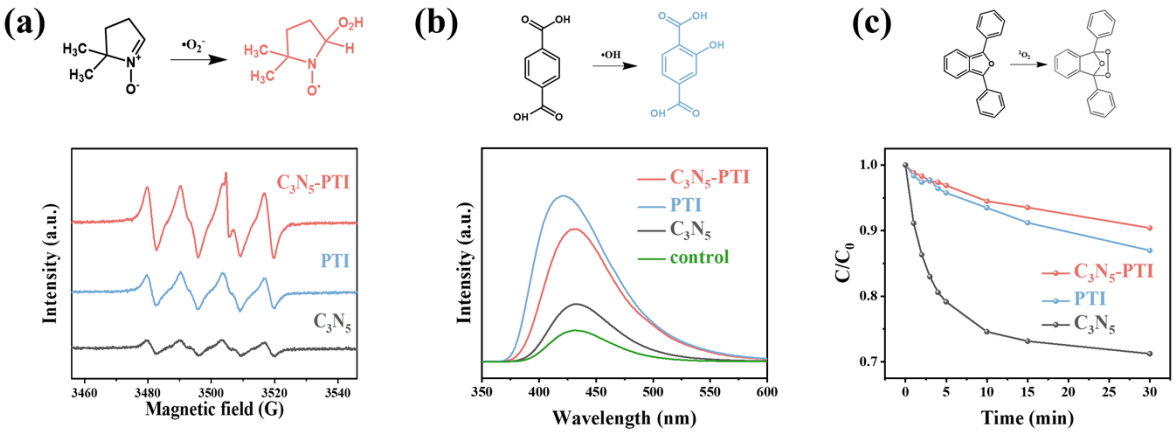

Fig. S7 (a) ESR spectra of C_3N_5-PTI, PTI and C_3N_5 obtained in the presence of DMPO as an electron-trapping agent. (b) Photoluminescence (PL) spectra of as-samples in the presence of terephthalic acid (excitation wavelength: 320 nm). (c) The degradation of DPBF in C_3N_5, PTI and C_3N_5-PTI systems.

Notes: As shown in Fig. S7, the dominant ROSs vary across different catalysts, which can be attributed to the following reasons. First, the oxidation potential of PTI is very positive (1.96 V), which is conductive to produce •OH through oxidation of H_2O (1.9 V). Secondly, the synthesis temperature of C_3N_5 material (520 °C) is relatively low in contrast to PTI (600 °C), and there are more surface functional groups, forming many defective states with low redox capability, which is unfavorable for charge transfer reactions for the production of •OH and$•O_2^-$ while promoting the $^1O_2$ production through energy transfer. Finally, for C_3N_5-PTI heterojunction, the charge transfer capability at the heterojunction interface is significantly enhanced, which facilitates the production of H_2O_2 through consecutive two-step single-electron reduction of O_2 (i.e., $O_2 + e^- \rightarrow •O_2^-$, $•O_2^- + e^- + 2H^+ \rightarrow H_2O_2$) and one-step two-electrons reduction of O_2 (i.e., $O_2 + e^- + 2H^+ \rightarrow H_2O_2$).

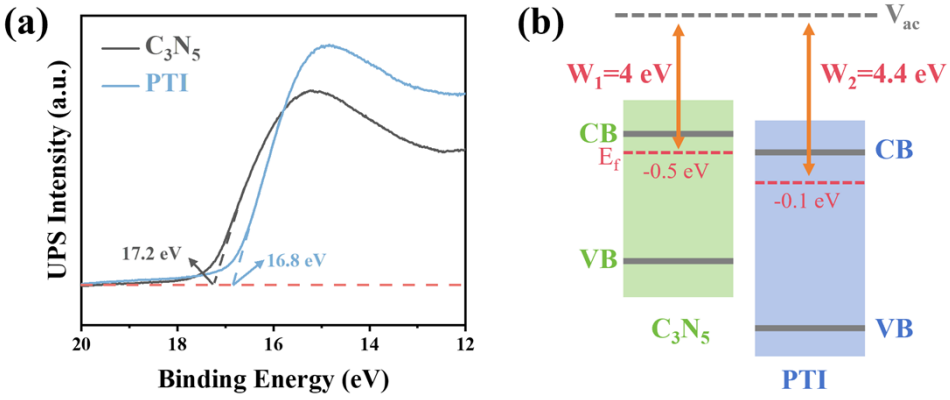

Fig. S8 (a) The UPS spectra of C_3N_5 and PTI, (b) Schematic illustration of the band positions for C_3N_5 and PTI.

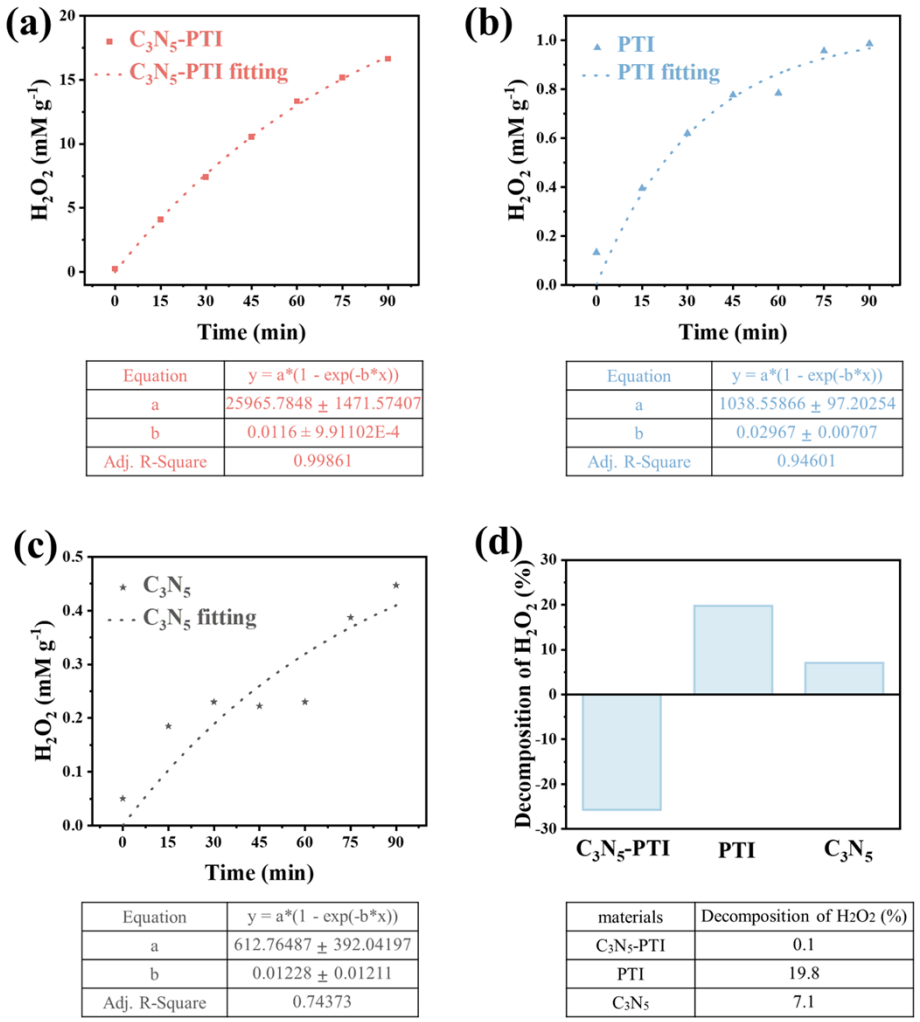

Equation	y = a*(1 - exp(-b*x))
a	25965.7848 ± 1471.57407
b	0.0116 ± 9.91102E-4
Adj. R-Square	0.99861

Equation	y = a*(1 - exp(-b*x))
a	1038.55866 ± 97.20254
b	0.02967 ± 0.00707
Adj. R-Square	0.94601

Equation	y = a*(1 - exp(-b*x))
a	612.76487 ± 392.04197
b	0.01228 ± 0.01211
Adj. R-Square	0.74373

materials	Decomposition of H_2O_2 (%)
C_3N_5-PTI	0.1
PTI	19.8
C_3N_5	7.1

Fig. S9 K_f, K_d fitting curve of (a) C_3N_5-PTI, (b) PTI and (c) C_3N_5, (d) H_2O_2 decomposition rate of the prepared samples. (y=[H_2O_2], a=K_f/K_d, b=K_d)

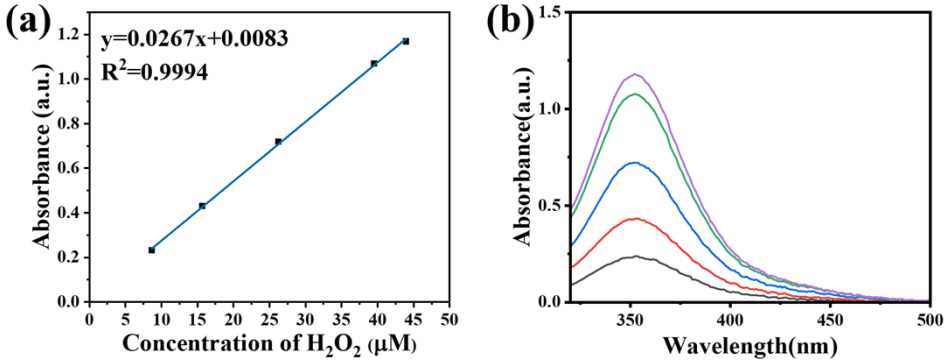

Fig. S10 (a) The linear relationship of concentration of H_2O_2 vs. UV-vis absorbance and (b) Standard curves for different concentration of H_2O_2

Equation S1:

$$\frac{1}{C^2} = \frac{2}{e\varepsilon\varepsilon_0 N_D}\left(-E + E_{fb} - \frac{KT}{e}\right) \qquad (1)$$

Where C, e, ε, ε_0, N_D, E, E_{fb}, K and T represent the capacitance of the space charge layer, the electron charge, the relative permittivity, the vacuum permittivity, the donor density, the applied potential, the flat-band potentials, the Boltzamann constant and the thermodynamic temperature, respectively.[9]

Equation S2:

$$[H_2O_2] = \frac{K_f}{K_d} \times \{1 - \exp(-K_d \times t)\} \qquad (2)$$

Where $[H_2O_2]$, K_f, K_d and t represent the hydrogen peroxide concentration, the formation rate constant, the decomposition rate constant, the reaction time, respectively. Zero-order and first-order kinetic studies were used to simulate the decomposition behavior of H_2O_2 on all samples.[10]

Table S1. Surface area and pore information of the prepared samples.

Samples	Surface area (m^2 g^{-1})	Adsorption cumulative volume (cm^3 g^{-1})	BJH Adsorption average pore width (nm)
C_3N_5	7.2638	0.07746	13.94
PTI	13.3457	0.166563	13.18
C_3N_5-PTI	55.6896	0.328717	8.12

Table S2. Comparison of photocatalytic H_2O_2 yields over different semiconductor catalysts.

Materials	Atmosphere	Formed H_2O_2	Reaction system	Irradiation conditions	Ref.
C_3N_5-PTI	Air	1675 μmol/g (90 min)	Catalyst: 5 mg Scavenger: 10 vol.% EtOH	5W white LED lamp (72.9 mW/cm^2)	This work
g-C_3N_4 Nanosheet	Air	43.07 μmol/g/h	Catalyst: 0.03 g Scavenger: IPA	λ=400-700 nm	11
C_3N_5/TiO_{2-x}	O_2	2.93 μmol/L/min	Catalyst: 4 cm^{-1} Scavenger: 10 vol.% EtOH	300 W Xe lamp	12
g-C_3N_4	O_2	170 μmol/L/h	Catalyst: 0.1 g	300 W Xe lamp	13
2%Bi/Bi_2O_3@g-C_3N_4	O_2	92.51 μmol/L/h	Catalyst: 50 mg	λ>420 nm	14
CN-S	O_2	201.45 μmol/g/h	Catalyst: 20 mg Scavenger: 0.1 mmol	20 W LED lamp (420 nm)	15
g-C_3N_4 nanosheets	O_2	1083 μmol/g/h	Catalyst: 0.05 g Scavenger: 10 vol.% EtOH	Simulated sunlight (filter: AM1.5)	16
CN/rGO@ BPQDs-0.04		181.69 μmol/L (3 h)	Catalyst: 50 mg	300 W Xe lamp (λ=420-780 nm)	17
g-C_3N_4/PDI	O_2	30 μmol (48 h)	Catalyst: 50 mg	λ>420 nm (26.9 W/m^2)	18
CN/Zn-OAC	O_2	77.5 μmol/h	Catalyst: 10 mg Scavenger: 20 vol.% EtOH	300 W Xe lamp (λ>400 nm)	19
C≡N─CN/IS/6% Ppy	O_2	895 μmol/L/h	Catalyst: 50 mg Scavenger: 10 vol.% IPA	300 W Xe lamp (λ>420 nm)	20
s-$B_{0.3}$CN	O_2	108.4 μM (2 h)	Catalyst: 30 mg	300 W Xe lamp (λ≥420 nm)	21
Cv-PCNNS	O_2	984.8 μmol/L/h	Catalyst: 50 mg Scavenger: 10 vol.% IPA	300 W Xe lamp (λ=420 nm, 140 mW/cm^2)	22
PCN-NV_C	O_2	25.1 μmol/h	Catalyst: 50 mg Scavenger: 10 vol.% MeOH	300 W Xe lamp (λ>420 nm)	23
UiO-66-B	O_2	1002 μmol/g/h	Catalyst: 30 mg/100 mL Scavenger: 10 vol.% IPA	300 W Xe lamp (filter: AM1.5)	24
NH_2-MIL-125	O_2	917 μmol/g/h	Catalyst: 5 mg/20 mL	500 W Xe lamp (λ>420 nm)	25
ZnO/PDA		1011.4 μmol/L/h	Catalyst: 20 mg/50 mL Scavenger: Glycol	300 W Xe lamp	26
Pd/A/$BiVO_4$	O_2	805.9 μmol/g/h	Catalyst: 100 mg/100 mL	300 W Xe lamp (λ>420 nm, 0.4 W/cm^2)	27
Au/WO_3		544 μM (5 h)	Catalyst: 50 mg/50 mL Scavenger: 4 vol.% CH_3OH	400 W metal halide lamp (λ≥420 nm, 4 mW/cm^2)	28
SI-PIL-TiO_2	O_2	1601 μmol/g/h	Catalyst: 10 mg/50 mL LEV	250 W Xe lamp	29
$CuFe_2O_4$/$ZnIn_2S_4$	O_2	2545.4 μmol/g	Catalyst: 1 g 50 mL ethanol+45 mL pure water	350 W Xe lamp (λ>420 nm)	30

References:

1 J. Yuan, N. Tian, Z. Zhu, W. Yu, M. Li, Y. Zhang, H. Huang, Chem. Eng. J., 2023, **467**, 143379.
2 F. He, Y. Lu, Y. Wu, S. Wang, Y. Zhang, P. Dong, Y. Wang, C. Zhao, S. Wang, J. Zhang, S. Wang, Adv. Mater., 2024, **36**, 2307490.
3 Y. Luo, C. Liu, J. Liu, X. Liu, Y. Zhou, X. Ou, B. Weng, J. Jiang, B. Han, Chem. Eng. J., 2024, **481**, 148494.
4 X. Liang, S. Xue, C. Yang, X. Ye, Y. Wang, Q. Chen, W. Lin, Y. Hou, G. Zhang, M. Shalom, Z. Yu, X. Wang, Angew. Chem. Int. Ed., 2023, **62**, e202216434.
5 Y. Shen, X. Du, Y. Shi, L.J. Nguetsa Kuate, Z. Chen, C. Zhu, L. Tan, F. Guo, S. Li, W. Shi, Adv. Powder Mat., 2024, **3**, 100202.
6 J. Yang, Y. Liang, K. Li, G. Yang, K. Wang, R. Xu, X. Xie, Appl. Catal. B, 2020, **262**, 118252.
7 B. Zhai, H. Li, G. Gao, Y. Wang, P. Niu, S. Wang, L. Li, Adv. Funct. Mater., 2022, **32**, 2207375.
8 H. Liang, A. Wang, R. Cheng, F. Chen, P. Kannan, C. Molochas, P. Tsiakaras, Chem. Eng. J., 2024, **489**, 151145.
9 J. Yang, Y. Liang, K. Li, G. Yang, K. Wang, R. Xu and X. Xie, Appl. Catal. B, 2020, **262**, 118252.
10 W. Liu, P. Wang, J. Chen, X. Gao, H. Che, B. Liu and Y. Ao, Adv. Funct. Mater., 2022, **32**, 2205119.
11 W. Liu, C. Song, M. Kou, Y. Wang, Y. Deng, T. Shimada and L. Ye, Chem. Eng. J., 2021, **425**, 130615.
12 W. Gan, X. Fu, J. Jin, J. Guo, M. Zhang, R. Chen, C. Ding, Y. Lu, J. Li and Z. Sun, J. Colloid Interface Sci., 2024, **653**, 1028-1039.
13 Z. Zhu, H. Pan, M. Murugananthan, J. Gong and Y. Zhang, Appl. Catal. B, 2018, **232**, 19-25.
14 X. Yan, G. Yu, C. Xing, Y. Hu, H. Liu and X. Li, Catal. Sci. Technol., 2023, **13**, 3094-3105.
15 B. Zhang, S. Wang, C. Qiu, Y. Xu and J. Zuo, Appl. Surf. Sci., 2022, **573**, 151506.
16 L. Zhou, J. Feng, B. Qiu, Y. Zhou, J. Lei, M. Xing, L. Wang, Y. Zhou, Y. Liu and J. Zhang, Appl. Catal. B, 2020, **267**, 118396.
17 J. Xiong, X. Li, J. Huang, X. Gao, Z. Chen, J. Liu, H. Li, B. Kang, W. Yao and Y. Zhu, Appl. Catal. B, 2020, **266**, 118602.
18 Y. Shiraishi, S. Kanazawa, Y. Kofuji, H. Sakamoto, S. Ichikawa, S. Tanaka and T. Hirai, Angew. Chem., Int. Ed., 2014, **53**, 13454-13459.
19 Y. Li, Y. Guo, G. Fan, D. Luan, X. Gu and X. Lou, Angew. Chem., Int. Ed., 2024, **63**, e202317572.
20 R. Li, K. Ba, D. Zhang, Y. Shi, C. Li, Y. Yu and M. Yang, Small, 2024, **20**, 2308568.
21 Z. Zhang, P. Luo, L. Gan, Y. Zhao, X. Wang, H. Peng and J. Peng, Appl. Surf. Sci., 2024, **649**, 159118.
22 R. Li, M. Zheng, X. Zhou, D. Zhang, Y. Shi, C. X. Li and M. Yang, Chem. Eng. J., 2023, **464**, 142584.
23 F. Lin, T. Wang, Z. Ren, X. Cai, Y. Wang, J. Chen, J. Wang, S. Zang, F. Mao and L. Lv, J. Colloid Interface Sci., 2023, **636**, 223-229.
24 Y. Li, F. Ma, L. Zheng, Y. Liu, Z. Wang, P. Wang, Z. Zheng, H. Cheng, Y. Dai, B. Huang, Mater. Horiz., 2021, **8**, 2842-2850.
25 Y. Zheng, H. Zhou, B. Zhou, J. Mao, Y. Zhao, Catal. Sci. Technol., 2022, **12**, 969-975.
26 G. Han, F. Xu, B. Cheng, Y. Li, J. Yu, L. Zhang, Acta Phys. - Chim. Sin., 2022, **38**, 1-10.
27 M. Sun, X. Wang, Y. Li, H. Pan, M. Murugananthan, Y. Han, J. Wu, M. Zhang, Y. Zhang, Z. Kang, ACS Catal., 2022, **12**, 2138-2149.
28 Y. Wang, Y. Wang, J. Zhao, M. Chen, X. Huang, Y. Xu, Appl. Catal. B Environ., 2021, **284**, 119691.
29 Y. Cheng, J. Jin, H. Yan, G. Zhou, Y. Xu, L. Tang, X. Liu, H. Li, K. Zhang, Z. Lu, Angew. Chem. Int. Ed., 2024, **63**, e202400857.
30 D. Liu, L. Jiang, D. Chen, Z. Hao, B. Deng, Y. Sun, X. Liu, B. Jia, L. Chen, H. Liu, Chem. Eng. J., 2024, **482**, 149165.